communications physics

A Nature Portfolio journal

Article

https://doi.org/10.1038/s42005-025-02128-8

Computational modelling of the semi-classical quantum vacuum in 3D

Zixin Zhang [1] ✉, Ramy Aboushelbaya[1], Iustin Ouatu[1], Elliott Denis[1], Abigail James[1], Robin J. L. Timmis [1], Marko W. Von Der Leyen[1], Peter A. Norreys [1,3], Rui Torres [2], Thomas Grismayer [2] & Luis O. Silva [2]

The global commissioning of multi-Petawatt laser systems provides unprecedented access to ultra-high electromagnetic fields for probing the quantum vacuum. However, current analytical models are limited, necessitating large-scale simulations for experimental validation. Here, we present real-time three-dimensional simulations of two quantum vacuum effects, using a semi-classical numerical solver based on the Heisenberg-Euler Lagrangian. The simulation model is benchmarked against vacuum birefringence analytical results with a counter-propagating setup. Simulations results of both plane-wave and Gaussian pulses are consistent with theoretical predictions. The solver is then applied to four-wave mixing using three Gaussian pulses with real-time information on the harmonic evolution. We provide quantitative explanations for the astigmatism in the output and produce precise estimates of the interaction time and size. Results are compared with the plane-wave model and previous numerical results. This solver paves the way for in-depth investigations of a broad spectrum of quantum vacuum effects in any arbitrary laser setup.

Quantum electrodynamics (QED) is one of the most fundamental and well-tested theories in Physics, validated by numerous precision tests[1–3]. One of the groundbreaking predictions of QED is on the nature of the vacuum, classically viewed as an empty space. The quantum vacuum is filled with energy fluctuations from which virtual electron-positron pairs arise. The presence of these virtual particles creates non-linearities in vacuum that interact with high power laser pulses propagating through, altering their properties. Examples of these interactions include vacuum birefringence[4–15], harmonic generation through four-wave mixing[16–24], photon splitting and merging[25–29], and quantum reflections[30].

There have been various indirect tests for photon-photon scattering, the underlying reaction for the above QED effects. These include the inelastic scattering experiment at Stanford University (1997) colliding an electron beam with terawatt laser pulses[31], the previously unsuccessful attempt of measuring photon-photon scattering via four-wave mixing (2000)[32], scattering of virtual photons at CERN using relativistic heavy-ion collisions (2017)[33], astrophysical observations on vacuum birefringence from neutron stars (2017)[8], and forward proton scattering in association with lepton pairs produced via photon fusion (2020)[34].

The advent of multi-petawatt lasers is able to bring us into a new regime of direct tests for real photon-photon scattering[35–37]. Currently, the Extreme Light Infrastructure (ELI) in Romania[38] is able to deliver two 10-PetaWatt (PW) laser beams along with a tunable gamma-ray beam. Amongst the near-future high-power lasers is the Vulcan 20-20 laser at the Central Laser Facility in the United Kingdom[39], which will produce a primary beam of 20 PW, as well as 8 beams with a combined energy of 20 kJ. The EP-OPAL project[40] at the University of Rochester in the United States plans on generating two beams, each of 25 PW. Photon-photon scattering via four-wave mixing has in fact been selected as one of the flagship experiments to be conducted in the future EP-OPAL facility[41]. Finally, the station of extreme light (SEL)[42] at Shanghai High repetition rate X-ray Free Laser and Extreme light facility (SHINE) in China are aiming at a 100 PW beam with a focused electric field strength up to 10^{15} V m^{-1}. This laser is also designed to combine with an X-ray free laser (XFEL) forexperiments such as vacuum birefringence. Unlike previous experiments, purely laser-based experiments provide a clean source of photons without interactions from other particles, significantly reducing experimental noise. These experiments will not only probe the quantum vacuum directly, but also provide tests for alternative theories such as Born-Infeld electrodynamics[43,44], axions[45–47] and millicharged particles[48].

While experimental conditions are increasingly promising with these up-coming facilities, current analytical models are somewhat limited to at most Gaussian beams under the paraxial approximation.

[1]Department of Physics, Atomic and Laser Physics Sub-Department, University of Oxford, Clarendon Laboratory, Parks Road, Oxford, OX13PU, UK. [2]GoLP/Instituto de Plasmas e Fusão Nuclear, Instituto Superior Técnico, Universidade de Lisboa, 1049-001 Lisbon, Portugal. [3]Present address: John Adams Institute for Accelerator Science, University of Oxford, Denys Wilkinson Building, Keble Road, Oxford, OX1 3RH, UK. ✉e-mail: zixin.zhang@physics.ox.ac.uk

In the context of four-wave mixing, work on analytical solutions was initially taken up by Lundin, Lundström et al. based on a plane-wave model[17,18,49]. Subsequent analytical work includes that by King et al. where the input beams are modelled as paraxial Gaussian beams under the infinite-Rayleigh-length approximation (IRLA)[19,21]. Berezin and Fedetov extended the analysis of IRLA Gaussian beams into an analytical formula for photon number yield for arbitrary interaction geometries[50]. In terms of vacuum birefringence, Gies, Karbstein et al. presented semi-analytical expressions for the signal photon distribution, using a leading-order paraxial expression for the pump beam, but an IRLA expression for the probe[12,51–54]. Implementation of generic and novel laser beam profiles have gained interest during the past decade[22,55,56], but analytical solutions are mostly obtained under approximations or limitations to special cases for simplification. This informs the need for more generic computational simulations to provide benchmarks for future experimental designs and real data sets.

There are currently two existing quantum vacuum simulation toolkits, HEWES by Lindner, Ölmez, and Ruhl[57], and the Vacuum Emission Picture solver by Blinne et al.[58–61]. Both are based on the Heisenberg-Euler (HE) effective Lagrangian. HEWES is an implicit Ordinary Differental Equation (ODE)-based solver for the semi-classical non-linear wave equation derived from the effective Lagrangian. The solver simulates both four-and six-photon processes and is able to achieve a high precision with ODE schemes up to thirteenth discretisation order, without spatial or temporal interpolation. However, currently the solver only models up to two paraxial Gaussian pulses, and performing three-dimensional simulations is challenging, especially with a high-order discretisation. On the other hand, the Vacuum Emission Picture solver calculates the laser-stimulated signal photon emission from the quantum vacuum. External fields are treated as a classical background, while the quantum vacuum signature is treated as signal photons. The solver is also coupled with a Maxwell solver to implement generic laser fields[60]. The nature of this numerical approach allows for an excellent signal-to-background separation. However, it also leads to the lack of inclusion of back-reactions into the driving laser fields, including QED-induced beam depletion. Additionally, this method computes only transition amplitudes to asymptotic states, limiting its ability to directly access real-time evolution within the interaction region.

This paper builds on the work presented in[62] on a Heisenberg-Euler solver based on a modified Yee scheme and extends the solver from one and two dimensions to three dimensions. The solver evaluates and propagates the fields using the non-linear Maxwell's equations derived from the HE Lagrangian. The numerical stability and robustness of the solver have been thoroughly tested in lower dimensions in[62]. This approach is implemented as part of OSIRIS[63], a highly parallel and fully relativistic particle-in-cell (PIC) code that has been extensively benchmarked against high-intensity laser-plasma interaction experiments, particularly those associated with laser-wakefield accelerators. Thanks to its integration into OSIRIS, the solver is able to simulate an arbitrary number of generic laser pulses that are not limited by the paraxial approximation. The solver provides the full real-time evolution and near-focal information of any simulated setup, allowing detailed physics investigations into the formation and evolution of the quantum vacuum signatures. Furthermore, the solver allows for greater flexibility in simulating a wide range of quantum phenomena[64–66], both in vacuum and in the presence of particles, as will naturally arise in experiments.

In this paper, the solver is incorporated into the latest version of OSIRIS. Its robustness in three dimensions is validated by benchmarking it against two quantum vacuum phenomena: vacuum birefringence and four-wave mixing. The simulation results show excellent agreement with both analytical results and past literature. Furthermore, the time-resolved capability of the solver provides insights into the temporal evolution of the interaction and reveals the underlying physics of the end-state results.

Methods

Theory

QED in vacuum can be approximated by the HE Lagrangian[67,68], as expressed below in Gaussian units:

$$\mathcal{L} = \frac{1}{8\pi}\left(E^2 - B^2\right) + \frac{\xi}{8\pi}\left[\left(E^2 - B^2\right)^2 + 7(\mathbf{E}\cdot\mathbf{B})^2\right], \tag{1}$$

where ξ is the non-linearity coupling parameter:

$$\xi = \frac{\hbar e^4}{45\pi m^4 c^7}. \tag{2}$$

This approximation holds under the conditions for fields $E \ll E_s$ and $\lambda \gg \lambda_c$, where $E_s = \frac{m_e^2 c^3}{e\hbar} \sim 10^{18}\,\mathrm{Vm}^{-1}$ is the Schwinger field, and $\lambda_c = \frac{\hbar}{mc} \sim 10^{-12}$ m is the Compton wavelength[69]. All simulations presented in this paper have fields and wavelengths strictly within these limits.

A set of semi-classical non-linear Maxwell's equations can be derived from the Lagrangian[70]:

$$\nabla\cdot\mathbf{E} = -4\pi\nabla\cdot\mathbf{P}, \tag{3}$$

$$\nabla\times\mathbf{E} + \frac{1}{c}\frac{\partial\mathbf{B}}{\partial t} = 0, \tag{4}$$

$$\nabla\cdot\mathbf{B} = 0, \tag{5}$$

$$\nabla\times\mathbf{B} - \frac{1}{c}\frac{\partial\mathbf{E}}{\partial t} = 4\pi\frac{1}{c}\frac{\partial\mathbf{P}}{\partial t} + 4\pi\nabla\times\mathbf{M}, \tag{6}$$

where one defines an effective polarisation $\mathbf{P}$ and magnetisation of the vacuum $\mathbf{M}$ as:

$$\mathbf{P} = \frac{\xi}{4\pi}\left[2\left(E^2 - B^2\right)\mathbf{E} + 7(\mathbf{E}\cdot\mathbf{B})\mathbf{B}\right], \tag{7}$$

$$\mathbf{M} = \frac{\xi}{4\pi}\left[-2\left(E^2 - B^2\right)\mathbf{B} + 7(\mathbf{E}\cdot\mathbf{B})\mathbf{E}\right]. \tag{8}$$

One also derives the non-linear wave equation

$$\left(\frac{\partial^2}{\partial t^2} - c^2\nabla^2\right)\mathbf{E} = 4\pi c^2\left[\nabla(\nabla\cdot\mathbf{P}) \quad -\frac{1}{c}\partial_t\left(\frac{1}{c}\partial_t\mathbf{P} + \nabla\times\mathbf{M}\right)\right]. \tag{9}$$

Under this formulation, the vacuum possesses non-linear electromagnetic properties and interacts with laser pulses propagating through it. The two effects of interest in this paper are vacuum birefringence and four-wave mixing. The following sections present an overview of the analytical solutions for the two effects, which will be compared to simulation results. For ease of comparison with experimental parameters, the following analytical expressions and later discussions are presented in SI units.

Vacuum birefringence. In vacuum birefringence[4–15], a probe pulse travelling through a strong electromagnetic background will experience a change in its refractive indices along different polarisations. The difference in refractive indices leads to dephasing between the different polarisation components. A linearly polarised pulse will thus gain a small ellipticity in its polarisation after passing through the strong background. In our simulations, the strong field is provided by an ultra-intense pump pulse, and the birefringence is extracted from a probe pulse that passes through the pump pulse[62,71]. The two pulses will be counter-propagating along the $\hat{\mathbf{x}}$-axis, both focusing at the origin.

Consider two scenarios. In the first scenario, both the pump and probe pulses are plane waves with a Gaussian temporal profile[71]:

$$\mathbf{E}(\mathbf{r},t)=\bar{\mathbf{E}}\cos(kx\pm\omega t)\exp\left(-\frac{(x\pm ct)^2}{2\sigma^2}\right), \tag{10}$$

where $\mathbf{E}$ is the pump and probe electric field profile, $\bar{\mathbf{E}}$ is the amplitude of the respective pulses, k and ω are their wave-numbers and frequencies, and σ is their longitudinal duration.

In the second scenario, both are finite-width Gaussian beams under the paraxial approximation[72], with focus at the origin:

$$\begin{aligned}\mathbf{E}(\mathbf{r},t)=\bar{\mathbf{E}}\frac{W_0}{W(x)}\exp\left(-\frac{y^2+z^2}{W^2(x)}\right)\cos(\Phi(\mathbf{r}))\\ \times\exp\left(-\frac{(x\pm ct)^2}{2\sigma^2}\right),\end{aligned} \tag{11}$$

where the phase Φ is given by

$$\Phi(\mathbf{r})=(kx\pm\omega t)+k\frac{y^2+z^2}{2R(x)}-\arctan\left(\frac{x}{z_0}\right). \tag{12}$$

W_0 is the beam waist of the pulse. The transverse extent of the pulse and its focusing effect are described by a longitudinal distance-dependent width $W(x)=W_0\sqrt{1+(\frac{x}{z_0})^2}$, where $z_0=\frac{\pi W_0^2}{\lambda}$ is the Rayleigh range of the pulse.

In the expressions presented below, the subscripts 0 and p designate the relevant parameters for the pump and the probe pulse respectively. In both cases, $\bar{E}_0\gg\bar{E}_\mathrm{p}$, such that the birefringent effect created by the probe pulse is considered negligible. For a probe pulse that is initially linearly polarised at θ, it will acquire a phase difference between its two components along $\hat{\mathbf{y}}$ and $\hat{\mathbf{z}}$ after the interaction:

$$\mathbf{E}_\mathrm{p}(x,t)=\frac{\bar{E}_\mathrm{p}}{2}\exp(-i\omega t)\exp(ik'x)\left[\cos(\theta)\exp(-i\Delta\phi)\mathbf{e}_y+\sin(\theta)\mathbf{e}_z\right]+\text{ c.c.} \tag{13}$$

where k' is the wave-number of the pulse after it passes through the pump, and $\Delta\phi$ is the phase difference given by[62,71]

$$\Delta\phi(\mathbf{r})=12\pi^{3/2}\xi\bar{E}_0^2k_\mathrm{p}\sigma_0\,\mathrm{erf}\left(\frac{x}{\sigma}\right) \tag{14}$$

for plane waves, and

$$\Delta\phi(\mathbf{r})=12\pi^{3/2}\xi\tilde{\bar{E}}_0^2(\mathbf{r})k_\mathrm{p}\sigma_0\,\mathrm{erf}\left(\frac{x}{\sigma}\right) \tag{15}$$

for paraxial Gaussian beams. c.c. denotes the complex conjugate of the first term. The term $\bar{E}_0^2$ given by

$$\tilde{\bar{E}}_0^2(\mathbf{r})=\frac{\bar{E}_0^2}{\left[1+\left(\frac{x}{z_0}\right)^2\right]}\exp\left(-2\frac{y^2+z^2}{W_0^2\left(1+\left(\frac{x}{z_0}\right)^2\right)}\right) \tag{16}$$

comes from a the modulus squared of the electric field strength of a transverse Gaussian profile. The longitudinal Gaussian profile integrates to the erf function. Finally, the ellipticity δ is related to the phase difference through

$$\delta=\frac{\sin 2\theta}{2}\tilde{\bar{E}}_\mathrm{p}\Delta\phi, \tag{17}$$

where

$$\tilde{\bar{E}}_\mathrm{p}(\mathbf{r})=\frac{\bar{E}_\mathrm{p}}{\sqrt{1+\left(\frac{x}{z_\mathrm{p}}\right)^2}}\exp\left(-\frac{y^2+z^2}{W_0^2\left(1+\left(\frac{x}{z_\mathrm{p}}\right)^2\right)}\right). \tag{18}$$

An additional signature of the quantum vacuum present in the interaction of tightly focused Gaussian beams is the diffraction spreading of output photons due to momentum transfer from the pump beam, and has been studied in recent years in[12,51–54]. For the simulations presented here where a relatively loosely focused pump pulse was used (the simulated pump pulse has a Rayleigh range 100 times greater than that used in[12]), the momentum transfer effects are considered negligible.

Four-wave mixing. Now consider three input plane waves with frequencies and wavevectors $(\omega_i,\mathbf{k}_i)$, where $i=1,2,3$. An output beam whose four-wavevector $(\omega_4,\ \mathbf{k}_4)$ satisfies the conservation of energy and momentum will be generated such that[49]:

$$\mathbf{k}_1+\mathbf{k}_2=\mathbf{k}_3+\mathbf{k}_4, \tag{19}$$

$$\omega_1+\omega_2=\omega_3+\omega_4. \tag{20}$$

In the present work, a two-dimensional interaction geometry is considered, where the wavevectors of all four waves are confined to the $\hat{\mathbf{x}}$-$\hat{\mathbf{y}}$ plane. The angles ϕ_i and γ_i are assigned to each field, where ϕ_i is defined as the angle $\mathbf{k}$ makes with the x-axis, and γ_i is the angle of polarisation from the z-axis, such that:

$$\mathbf{k_i}=k_i\cos\phi_i\hat{\mathbf{x}}+k_i\sin\phi_i\hat{\mathbf{y}}, \tag{21}$$

$$\mathbf{E}_i(\mathbf{r},t)=E_i(\mathbf{r},t)\left[\sin\gamma_i\sin\phi_i\hat{\mathbf{x}}-\sin\gamma_i\cos\phi_i\hat{\mathbf{y}}+\cos\gamma_i\hat{\mathbf{z}}\right]. \tag{22}$$

Incoming beams are approximated as top-hat beams confined by length L, width and height b ($L>b$). It is further approximated that during the interaction process, the pulses interact in a cubic region with volume b^3. The interaction region is assumed to exist for a limited period of time, determined by the duration of the pulse $\frac{L}{c}$. Any edge-effects are considered negligible in the model. The output electric field then takes the form[49]

$$\mathbf{E}_\mathrm{out}(\mathbf{r},t)=E_0(r,\theta,\phi)\cos(k_4r-\omega_4t+\delta)\mathbf{G}_\mathrm{2d}, \tag{23}$$

where

$$\begin{aligned}E_0(r,\theta,\phi)=&\frac{1}{4\pi\epsilon_0}\frac{8\xi}{k_4\pi r}\frac{\sin\left(k_4\frac{b}{2}(\cos\phi_4-\cos\phi\sin\theta)\right)}{\cos\phi_4-\cos\phi\sin\theta}\\ &\frac{\sin\left(k_4\frac{b}{2}(\sin\phi_4-\sin\phi\sin\theta)\right)}{\sin\phi_4-\sin\phi\sin\theta}\frac{\sin\left(k_4\frac{b}{2}\cos\theta\right)}{\cos\theta}\\ &E_1E_2E_3,\end{aligned} \tag{24}$$

r, θ and ϕ are conventional spherical coordinates, with the origin at the interaction centre. δ is a constant phase. $\mathbf{G}_\mathrm{2d}$ is a geometric factor that depends on the interaction geometry and polarisation of input pulses, and its full expression is given by Supplementary Note 1.

The output power can be calculated by integrating the intensity over a spherical shell, which gives

$$P_\mathrm{out}=\frac{4\xi^2}{c^2\epsilon_0^4}\left(\frac{1}{\lambda_4}\right)^4G_\mathrm{2d}^2\alpha^2P_1P_2P_3, \tag{25}$$

with α^2 given by[17]

$$\alpha^2 = \frac{64}{k_4^4 b^6}\int_0^{2\pi}\int_0^{\pi}\frac{\sin^2\left[k_4 b f(\theta,\phi)/2\right]\sin^2\left[k_4 b g(\theta,\phi)/2\right]}{f^2(\theta,\phi)g^2(\theta,\phi)} \times \frac{\sin^2\left[k_4\frac{b}{2}\cos\theta\right]}{\cos^2\theta}\sin\theta\, d\theta\, d\phi, \tag{26}$$

where $f(\theta,\phi) = 1-\cos\phi\sin\theta$ and $g(\theta,\phi) = \sin\phi\sin\theta$. G_{2d} is the modulus of $\mathbf{G}_{2d}$. $P_{1,2,3}$ represent the power of the input pulses. The expected number of photons obtained per shot (N_{out}) is calculated by multiplying the power by the time duration and dividing by the output photon energy:

$$N_{out} = \frac{2\xi^2}{\pi c^4 \epsilon_0^4 \hbar}\left(\frac{1}{\lambda_4}\right)^3 G_{2d}^2 \alpha^2 L P_1 P_2 P_3. \tag{27}$$

Semi-classical QED solver

The Yee scheme[73,74] is a widely used solver for Maxwell's equations, wherein the electric and magnetic fields are computed on a staggered grid (See Supplementary Fig. anchorlinkdmmc11). To address the non-linearities in the modified Maxwell's equations, the solver employs a modified Yee scheme[62] (See Supplementary Fig. anchorlinkdmmc12 for a summary of the below process). At each time step t_n:

- The standard Yee scheme, based on the original Maxwell's equations in the classical vacuum, is carried out to compute the electric and magnetic fields at staggered locations at t_{n+1}.
- Given that the non-linearities couple to all components of electromagnetic fields, the field values are linearly interpolated to all grid locations.
- The two electromagnetic invariants, $E^2 - B^2$ and $\mathbf{E}\cdot\mathbf{B}$ are calculated at all grid locations at t_{n+1}.
- The effective polarisation (Eq. (7)) and magnetisation (Eq. (8)) are calculated at all grid locations at t_{n+1}.
- The electric field at t_{n+1} is then re-evaluated using the modified Ampere's Law (Eq. (6)).
- The updated electric field is used to revise the polarisation and magnetisation terms, which in turn update the electric field (Eq. (4)). The iterative process continues until convergence to the desired accuracy is achieved.
- The magnetic field at t_{n+1} is then re-calculated using the modified Faraday's Law (Eq. (4)).

This scheme has the important advantage that it can be straightforwardly incorporated into the electromagnetic solver in PIC code, and allows the calculation of quantum vacuum effects in the existing PIC code algorithm without significant modifications. The solver has been upgraded to be compatible with the latest version of OSIRIS, which supports new features such as non-paraxial pulses and pulse propagation at an angle[75], and benefits from a shorter run-time. For the simulation of vacuum birefringence, a spatial resolution of $\frac{1}{33}$ of the probe pulse wavelength is adopted along its propagation direction, and $\frac{1}{15}$ of the beam width is used transversely. For four-wave mixing, to resolve the propagation of the pulses at an angle, the spatial resolution is set to $\frac{1}{30}$ of the wavelength on the $\hat{\mathbf{x}}$-$\hat{\mathbf{y}}$ plane, and $\frac{1}{10}$ along $\hat{\mathbf{z}}$. With the specified resolution, the simulation of vacuum birefringence with two plane-wave pulses took approximately 0.5 hour to complete without quantum effects, and 15 hours with the addition of the quantum vacuum solver, using the same computational resources. The simulations of four-wave mixing took 0.75 and 3.4 hours without and with the solver. The reasonable runtime allows for higher flexibility in running multiple simulations, for example when carrying out parameter scans.

Results

Vacuum birefringence

The stability and accuracy of the solver in 1D and 2D have been validated in[62]. Here the benchmarking was extended to vacuum birefringence in 3D for the two scenarios outlined in Eq. (10) and Eq. (11). To enhance the non-linear effects, the value of the non-linearity coupling parameter ξ in Eq. (7) and Eq. (8) was artificially increased from $\sim 10^{-51}$ to 10^{-44}. One notes that this adjustment only re-scales the results to increase signal-to-noise ratio without introducing additional physical effects. To obtain a realistic estimate of the physical quantities, only a re-scaling based on ξ is needed. All diagnostic calculations are performed using $\mathbf{E}$ and $\mathbf{B}$ fields interpolated to the cell centre.

The standard counter-propagating setup, shown in Fig. 1, consists of an optical pump pulse and an X-ray probe pulse. The two pulses share the same focal spot, duration and beam width, and fully overlap at focus. The pulse parameters for both scenarios are detailed in Table 1. The ellipticity value is measured from the polarisation plane of the probe pulse at a fixed location.

Results for the ellipticity obtained in the plane-wave case are plotted as a ratio of the theoretical prediction (Eq. (14)) across the transverse plane, as shown in Fig. 2 (a). The maximum deviation from theory is 2.9%, demonstrating excellent agreement. There is a variation in the ratio within a range of 3.9% across the transverse plane, demonstrating the robustness of the solver across the $\hat{\mathbf{y}}$-$\hat{\mathbf{z}}$ plane.

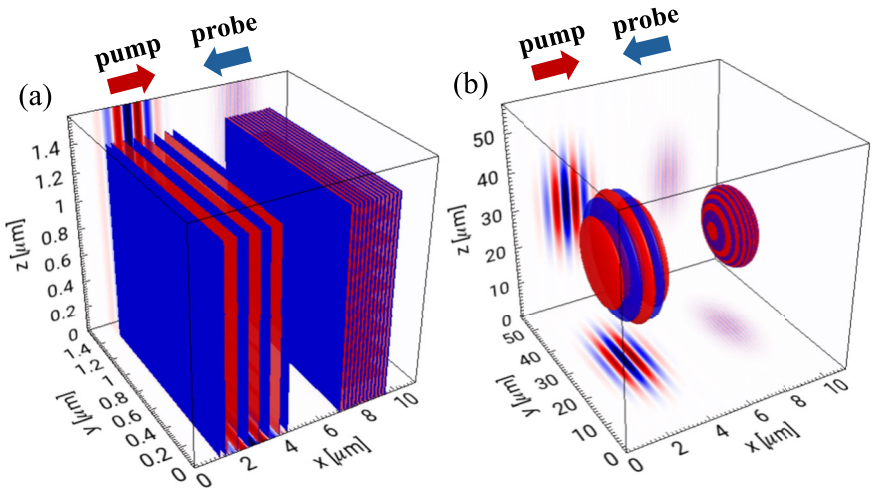

Fig. 1 | A schematic view of the vacuum birefringence setup. A counter-propagating probe and pump setup is simulated in 3D: **a** both probe and pump pulses are plane waves; **b** both are Gaussian beams. Different colors represent different iso-surfaces of electric field strengths. The relative wavelengths and electric field strengths in the figure are not to scale, with the accurate parameters shown in Table 1.

Table 1 | Input parameters for pump and probe pulse in vacuum birefringence setup

Pulse	λ (nm)	E_0 (Vm^{-1})	σ (fs)	$W_{Gaussian}$ (μm)
Pump	1000	8.6×10^{14}	2.1	9.6
Probe	10	3.2×10^{12}	2.1	9.6

The plane-wave and Gaussian scenarios share the same wavelength λ, peak electric field at focus E_0 and temporal duration σ. Plane waves are simulated to have an infinite spatial extent that spans the simulation box, while Gaussians have a beam waist W specified in the table.

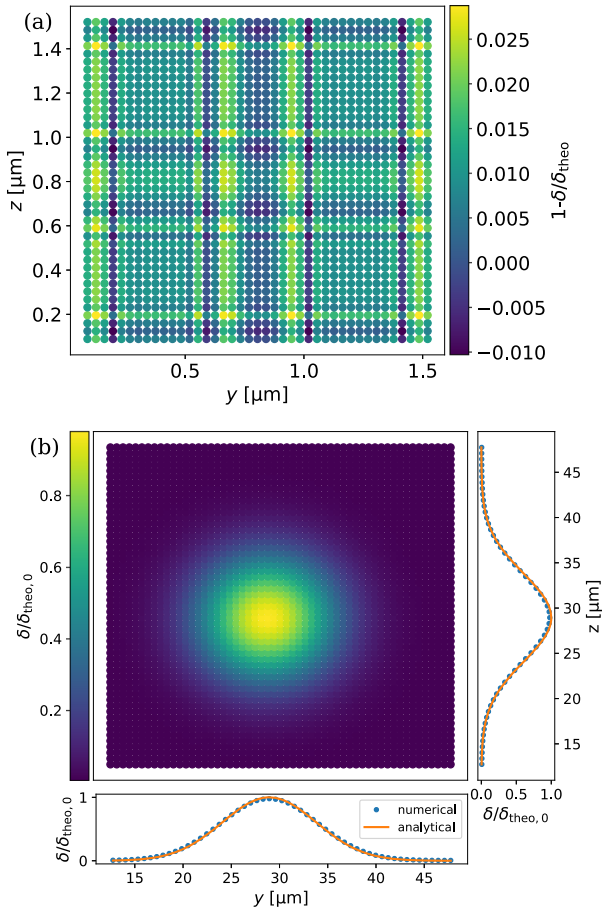

Fig. 2 | Simulation ellipticity δ relative to theoretical predictions δ_{theo}. **a** Percentage deviation of δ from δ_{theo} across the transverse plane of the probe pulse for plane-wave scenario. Maximum deviation from the theoretical prediction is 2.9%, with a variation of 3.9% across the plane; **b** Normalised ellipticity across the transverse plane for the Gaussian scenario. $\delta_{theo,0} \equiv \delta_{theo}(y = z = 30\,\mu m)$ is the theoretically predicted value for peak ellipticity. Line outs are taken along $\hat{\mathbf{y}}$ and $\hat{\mathbf{z}}$-axis at central $\hat{\mathbf{y}}$ and $\hat{\mathbf{z}}$ locations (30 μm). Deviation from theoretical value at the peak is 2.1%.

For the Gaussian setup (Fig.1b), the ellipticity is expected to mirror the Gaussian profile of the pump pulse across the $\hat{\mathbf{y}}$-$\hat{\mathbf{z}}$ plane, as shown in Fig. 2. Comparison with theory is shown in slices along the central $\hat{\mathbf{y}}$ and $\hat{\mathbf{z}}$ axes. The deviation from theory at the peak of the Gaussian is 2.1% and is found to be resolution dependent. Increasing the y-z plane resolution by 1.8 times reduces the deviation to 1.7%. The deviation from analytical predictions for both scenarios is consistent with previous deviations obtained in past literature when the solver was benchmarked in two dimensions[71], validating the continued accuracy of the solver when extended to three dimensions.

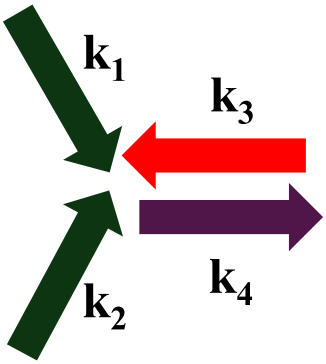

Fig. 3 | A schematic view of the four-wave mixing set up. A two-dimensional interaction geometry is simulated, where the wave-vectors of all four beams lie on the $\hat{\mathbf{x}} - \hat{\mathbf{y}}$ plane. The four beams have a wavelength of 0.5μm (λ_1 and λ_2), 1μm (λ_3) and 0.3μm (λ_4). The colouring reflects the respective wavelengths.

Table 2 | Input parameters for the three input pulses in four-wave mixing

λ_1 (μm)	λ_2 (μm)	λ_3 (μm)	λ_4 (μm)
0.5	0.5	1	0.33
E_0 (Vm^{-1})	P_0 (PW)	σ (fs)	W (μm)
6.4×10^{14}	13.9	11.2	4.0

The input beams have different wavelengths λ, but share the same peak electric field at focus E_0, temporal duration σ and beam waist W. For ease of comparison with other literature, the peak power of each beam at focus P_0 is also shown.

Four-wave mixing

The particular geometry studied here is

$$\begin{cases} \mathbf{k}_1 = -k\hat{\mathbf{x}} - \sqrt{3}k\hat{\mathbf{y}} \\ \mathbf{k}_2 = -k\hat{\mathbf{x}} + \sqrt{3}k\hat{\mathbf{y}} \\ \mathbf{k}_3 = k\hat{\mathbf{x}} \\ \mathbf{k}_4 = -3k\hat{\mathbf{x}} \end{cases}, \tag{28}$$

as shown by Fig. 3, reproducing the setup studied theoretically in Refs. 17,22. The output beam is well-separated from the three incoming beams, making detection straightforward. This geometry also yields a reasonable number of photons compared to other potential setups[49].

The plane-wave model is physically unrealistic and offers limited insight for future experiments. Therefore, in our simulation, all three beams have realistic Gaussian profiles. The input beams each have a wavelength of 0.5 μm (λ_1 and λ_2) and 1 μm (λ_3). They share the same electric field strength, pulse duration and beam width, as shown by Table 2. This geometry yields a third harmonic output pulse with a wavelength of 0.3 μm (λ_4). The simplest polarisation configuration was first simulated: all three input beams are polarised along the $\hat{\mathbf{z}}$-axis. The time-resolved feature of the solver allows one to visualise and analyse the interaction process at any time step (See Supplementary Fig. anchorlinkdmmc13 for snapshots of the simulation). A first deviation from the plane-wave model is already observed by looking at the interaction region at $\omega t = 100$ (Fig. 4), which corresponds to the mid-point of the simulation where maximal overlap between the input beams occurs. The region shown is defined to include all points whose local field strength exceeds half of the peak field strength, thus highlighting the regions of significant non-linearities. It can be clearly seen that the region fits more to an ellipsoid than the cube assumed by the plane-wave model. A surface fit gives the radii along $\hat{\mathbf{x}}$, $\hat{\mathbf{y}}$, and $\hat{\mathbf{z}}$ as 3.43μm, 3.51μm and 3.35μm. Such insights are helpful for prospective experimental designs on vacuum chamber dimensions for four-wave mixing setups.

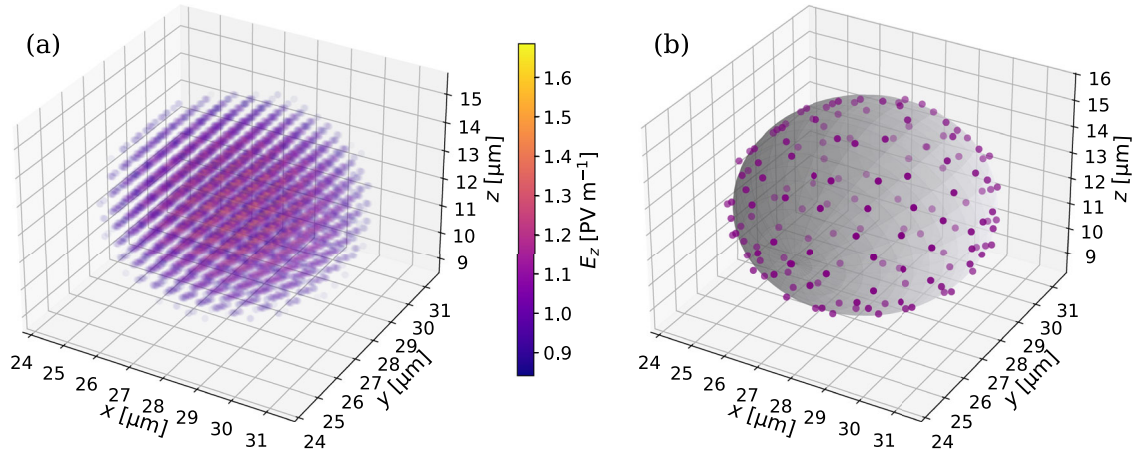

Fig. 4 | The interaction region at $\omega t = 100$ in three dimensions. The region is defined by the spatial envelope where the local field strength exceeds half of the peak field strength. **a** All the points in space satisfying the criterion. The colour-coding represents the local electric field strength; (**b**) includes only the points near the outer surface, and the ellipsoid fit.

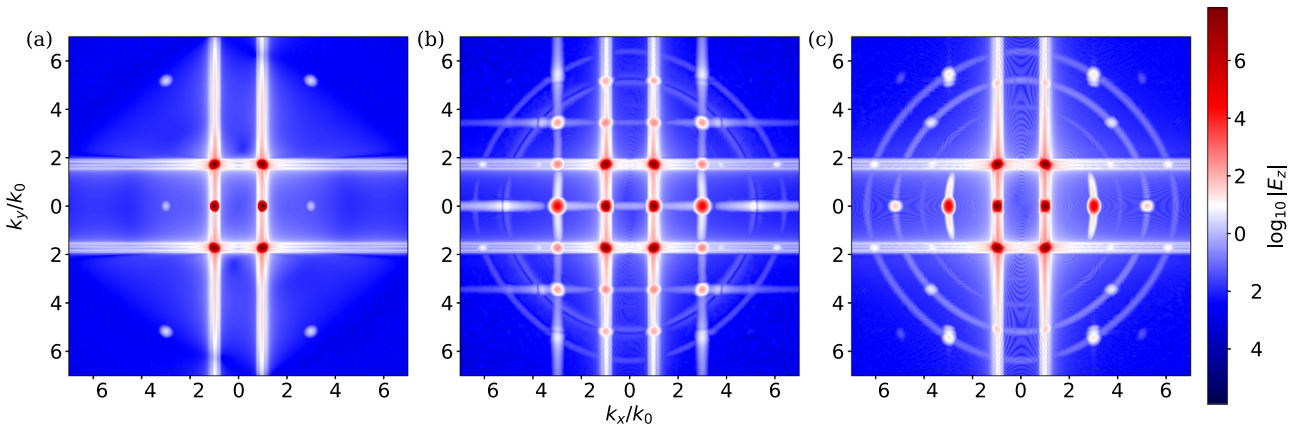

Fig. 5 | Fast Fourier Transforms of the electric field E_z in the x-y plane at three stages of the simulation. The Fourier Transformed field is plotted on a $\log_{10}$ scale. Multiple harmonics can be identified in ωt = (**a**) 1, **b** 100 and **c** 200. k values are normalised by the fundamental wavenumber k_0, which corresponds to the fundamental frequency ω. The initial harmonics in (**a**) are produced from self-interaction of the input beams. Harmonics produced from four-wave mixing are presented at (**b**), consistent with simple harmonic analysis. The third harmonics at $(\pm 3k_0, 0)$ remain the highest intensity among all higher harmonics throughout the interaction. The real time evolution is shown by Supplementary Movie 1.

Figure 5 shows the resulting Fast Fourier Transforms (FFT) in the $\hat{\mathbf{x}}$-$\hat{\mathbf{y}}$ plane at three stages, ωt = (a) 0, (b) 100 and (c) 200, which corresponds to the start, the mid-point and the end of the simulation. Tracking the evolution of the phase space allows one to identify the range of harmonics produced throughout the simulation. The six highest-intensity harmonics at locations $(k_x, k_y) = (\pm k_0, 0)$ and $(\pm k_0, \pm\sqrt{3}k_0)$ represent the three input beams. The harmonics are smeared out around the central frequencies due to finite pulse sizes. The white strips along k_x and k_y arise from imperfections in pulse propagation in the simulation, but are easily separable from the desired third harmonic due to intensity differences. From Fig.5 (a) one can see the harmonics at $(\pm 3k_0, 0)$ and $(\pm 3k_0, \pm 3\sqrt{3}k_0)$ arising due to self-interaction of the input beams[71]. One notes that self-interaction occurs only in non-plane-wave pulses, where the curvature of the wave fronts induces photon-photon scattering within the pulse itself. Mathematically, this can also be straightforwardly seen from the two invariants $E^2 - B^2$ and $\mathbf{E} \cdot \mathbf{B}$ contained in the non-linear terms in Eqs. (7) and (8), which are exactly zero for plane waves. This is hence not captured in the plane-wave model. The harmonics produced from the three-beam interaction are presented by Fig. 5b. From Eq. (9), one can see that the output electric field includes the frequency components present in the non-linear source term, which scales as E^3. Substituting the input field as:

$$\mathbf{E}(\mathbf{r},t) = \Big(\mathbf{E}_1(\mathbf{r},t)\mathrm{e}^{-ikx} + \mathbf{E}_2(\mathbf{r},t)\mathrm{e}^{-ik(x+\sqrt{3}y)} + \mathbf{E}_3(\mathbf{r},t)\mathrm{e}^{-ik(x-\sqrt{3}y)}\Big) + c.c. \tag{29}$$

into Eq. (9) gives a range of harmonics including $(\pm k_0, \pm 2\sqrt{3}k_0)$, $(\pm k_0, \pm 3\sqrt{3}k_0)$, $(\pm 3k_0, 0)$, $(\pm 3k_0, \pm\sqrt{3}k_0)$ and $(\pm 3k_0, \pm 2\sqrt{3}k_0)$. However, most of these modes are off-shell, i.e. they only satisfy the conservation of momentum but not energy. Therefore, the intensities of harmonics at $(\pm k_0, \pm 2\sqrt{3}k_0)$, $(\pm 3k_0, \pm\sqrt{3}k_0)$ and $(\pm 3k_0, \pm 2\sqrt{3}k_0)$ decay with time and they are no longer present approaching the end of the simulation, suggesting their evanescent nature. The interesting presence of these harmonics might contribute to additional quantum signatures in a single experiment that are discernible from the input pulses in frequency. Their evolution is often overlooked in analytical expressions that focus solely on the on-shell harmonic output, yet they offer new opportunities for investigating evanescent fields within the interaction. In this context, the

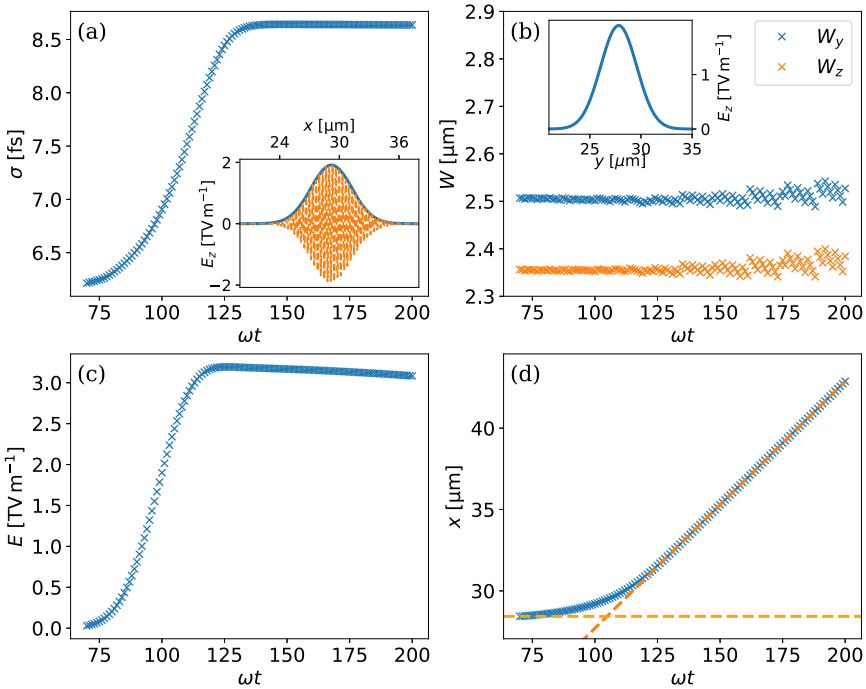

Fig. 6 | Temporal evolution of the output third harmonic. The evolution of (**a**) the output pulses's longitudinal duration; **b** the transverse widths along $\hat{\mathbf{y}}$ and $\hat{\mathbf{z}}$; **c** the peak electric field strength and (**d**) the location of the peak allows one to identify important time scales in the simulation. The insets in (**a**) and (**b**) show the profile of the output pulse along $\hat{\mathbf{x}}$ and $\hat{\mathbf{y}}$ at $\omega t = 100$. The blue line in the inset in (**a**) is a Gaussian fit to the envelope of the pulse. The two orange dashed lines in (**d**) are asymptotes of a stationary peak, and one which propagates at a constant speed $\simeq 0.99c$.

time-resolved capability of the solver is valuable for providing quantitative descriptions of the full spectrum of harmonics that emerge throughout the interaction process. On the other hand, the third harmonic's intensity stays relatively constant. The difference in intensities and frequencies allows the straightforward separation of the third harmonic from the other frequency components. These plots align with the principle of the four-wave mixing experiment, which is used to stimulate the generation of this particular harmonic.

The resulting output pulse, extracted by a frequency filter, also exhibits a Gaussian profile, as shown by the insets in Fig. 6a, b. The output pulse is polarised along the $\hat{\mathbf{z}}$-axis, consistent with the theoretical predictions. The solver also allows one to gain insights into its evolution. Figure 6 illustrates the evolution of several key characteristics. A similar transition is seen in the pulse length and peak field strength. The generation process begins before ωt = 100, when considerable pulse overlap occurs. Both follow an exponential-like increase until reaching a maximum at ωt = 126, coinciding with the separation of the input pulses. Beyond this point, the peak field strength decreases due to the pulse spreading in vacuum, as evidenced by the gradual increase in transverse width shown in Figure 6b, while its length remains constant. This enables the identification of an asymptotic time beyond which the pulse propagates classically, without further nonlinear interactions. The asymptotic length of the output pulse is shorter than the input ones, with $\sigma \sim 8.6fs$. It is also smaller in size and slightly astigmatic, with $W \sim 2.51\mu$m along the $\hat{\mathbf{y}}$-axis, and 2.37μm along the $\hat{\mathbf{z}}$-axis. The astigmatism comes from the asymmetry in the interaction geometry. When the beams approach each other at oblique incidence, the overlap region along the two axes is asymmetric. Specifically, the interaction length along the $\hat{\mathbf{y}}$-axis is determined by both the transverse width and length of the input pulses, while the interaction length along the $\hat{\mathbf{z}}$-axis is dependent only on their width. In the current simulation settings, the pulses' length is slightly larger than their width, suggesting that the output pulse may have a slightly greater width along $\hat{\mathbf{y}}$. Astigmatism is ignored in the plane-wave model, while deviations from this approximation are evident in the overlap region shown in Fig. 4. A similar asymmetry was observed in ref. 59 for a different interaction geometry. Here, a more quantitative basis is given by comparing the interaction lengths along the two axes in Fig. 4. The full-width-at-half-maximum (FWHM), given by the diameters of the fitted ellipsoid, is 7.0 μm along $\hat{\mathbf{y}}$ and 6.7μm along $\hat{\mathbf{z}}$, supporting the hypothesis that astigmatism in the output signal originates from the interaction region. This highlights the solver's capability to trace output characteristics back to their physical origins at any time step.

A particularly intriguing observation from the simulation results is the transition in the peak location of the generated third harmonic. During the interaction process, there is a continuous transition from the peak staying nearly stationary as the pulse is being generated, to propagating at a constant speed. The change in group velocity reflects the evolving effective refractive index of the quantum vacuum, an effect that is qualitatively expected due to the separation of the driving pulses but has not been explicitly resolved in previous studies. Similar to Fig. 6a, c, the transition completes near $\omega t = 126$. The asymptotic propagation speed of the generated pulse, measured from the slope, is $0.99c$. These findings enable precise estimates of interaction durations and propagation times to a detector, which are crucial for experimental setups employing time-gated photon detectors to enhance signal-to-noise ratio. For example, the peak of the output pulse reaches a position 16 μm from the interaction point 106s after the simulation starts. Considering that the pulse has reached the asymptotic stage where it can be modelled classically, these graphs can be extrapolated to give some initial estimates of a detection window. For a detector 10cm away, it takes 0.34ns for the peak to reach the detector, with a 21fs window determined from the pulse's FWHM. This highlights the solver's distinct advantage in identifying and predicting key time points, compared to previous analytical and numerical approaches that focus solely on asymptotic results.

Comparing with analytical results from the plane-wave model[17] requires normalisation. Here, two different methods have been adopted. As Eq. (25) and Eq. (27) suggest, four-wave mixing is a local interaction process, where the power and energy of the output pulse is directly proportional to the power of the input pulses. Hence, in the first method, the input power of the plane waves is matched with the peak power of Gaussian pulses in the simulations. The width (b) of the plane waves is approximated by an effective width of the Gaussian pulses given by $\sqrt{\pi}W$. Similarly, the effective time duration of the pulses is $\sqrt{2\pi}\sigma$. The choices of the effective width and duration are kept consistent with[19], where a similar comparison to the plane-wave model was carried out. However, in light of future experiments, where the pulse energy is the main parameter that can be controlled, in the second method, the total energy of each plane wave is matched to that of the input pulse in the simulations. This also allows one to compare straightforwardly

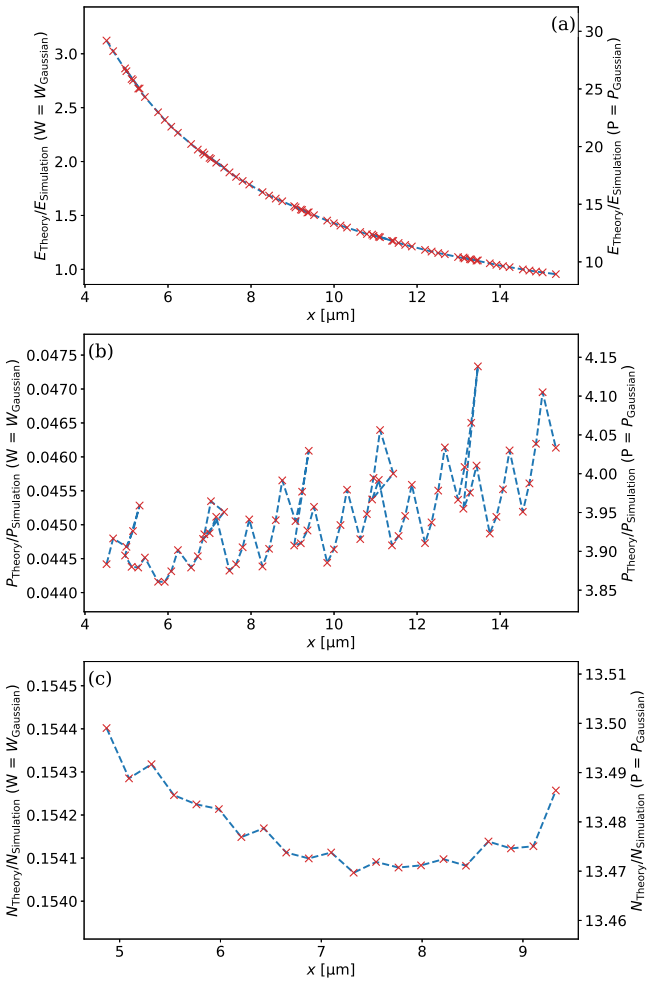

Fig. 7 | Ratios of analytical results to simulation results for output pulse properties. The ratios of (**a**) peak electric field, **b** peak power, **c** total number of photons are plotted against distance from the interaction point (also the focus). The simulation results are represented by crosses, and the dashed lines represent trend lines. Two axes are shown with different normalisation methods, scaled by a constant factor. The left axis represents the ratio when the plane-wave model input energy is matched with that of each input pulse in the simulation. The right axis represents when the plane-wave model input power is matched with the peak power of each input pulse in the simulation. Analytical results for the output electric field overshoot close to the interaction point, while ratios of power and photon number remain nearly constant with distance.

with the results obtained by the Vacuum Emission Picture solver in[59], where the same method was used. Given the use of input pulse powers in Eqs. (23), (25), (27)), the input pulse energy is converted into an effective power given by $P_{eff} = \frac{J}{\sqrt{2\pi}\sigma}$, where J is the input pulse energy. The effective power calculated is 5PW, compared with the peak power of the simulated Gaussians ~ 14PW.

Before discussing the results, it is worth noting again the main assumptions in the plane-wave model: (a) Both the input and output beams are assumed to have a top-hat transverse and longitudinal profile, with a constant electric field strength in the region confined by their lengths and widths; (b) The interaction region is assumed as a cube that exists for a limited period of time determined by the input pulse duration; (c) All end-effects at the edges of the pulses are ignored; (d) In deriving Eq. (23), it is assumed that the detector (observer) distance $r \gg L$. These points will be referred back to when explaining the various differences from theory.

First, one compares the on-axis electric field, peak power of the output pulse and the total number of photons emitted per interaction with the plane-wave model predictions. Figure 7 represents the ratio of theoretical to simulation results for the respective quantities against the detector distance from the interaction point. The right axis represents method 1, where input power is matched. The left axis represents method 2, where input energy is matched. Starting with method 1, on average, there is a factor of 3.9 difference between theory and simulation results for the output peak power, while the photon number ratio reaches 13.5. The O(1) difference in power shows that the plane-wave model provides a reasonably good estimate of the output power, for input pulses that fall under the paraxial approximation. Differences can be attributed to point (b) raised above, the over-simplification of the interaction region, and (c), the lack of treatment of end-effects. The larger discrepancy in photon number is justified by point (a), since theory assumes plane-wave inputs with a constant power, whereas the power of Gaussian pulses falls off rapidly away from the peak position. This result is also consistent with[19], where King et al. demonstrated that implementing more realistic input laser profiles predicts a lower photon number than the plane-wave model, under the power matching method. The biggest variation is found in the on-axis electric field ratio, which drops progressively with detector distance. This aligns with point (d) given that the length scale investigated here is of the same order as the pulse length, and thus is outside the validity of the assumption. The dropping discrepancy as the detector is placed further away is also justified by (d). This marks the success of the simulation to produce more accurate results at near-focal locations than analytical predictions. The ratios of power and photon number are also analysed at various distances from the interaction point to assess the consistency of the simulation results. The output power shows a maximum variation of 7.0% in a range of 11 μm, while the photon number ratio varies by up to 0.2% in 4.5 μm, further demonstrating the robustness of the solver to propagate the output pulse in space and time without numerical diffraction effects.

Looking at method 2, one notes that with energy matching, realistic Gaussian pulses are actually able to generate a stronger signal than the plane-wave model predicts. A justification for this result has been suggested first in ref. 58, which suggests that the signal depends decisively on the peak field strengths of the input pulses. Plane wave pulses have a more even distribution of energy than Gaussians, so for the same energy, it naturally follows that plane waves have a lower electric field strength than the peak of the Gaussians. The simulations results are also consistent with the results in ref. 59. In particular, the obtained output photon number is a factor of six greater than the theoretical prediction on average. This is in good agreement with the results presented in ref. 59, where a different interaction geometry was investigated using paraxial Gaussian pulses in four-wave mixing, and the resulting photon number was a factor of two to three bigger than the plane-wave prediction. The potential differences between these results are attributed to the different interaction geometry and pulse sizes. The photon number ratio also depends on how the effective pulse duration is defined and calculated. Finally, upon rescaling ξ back to its actual value while maintaining the rest of the parameters used in the simulation, a photon number of 156 is achieved with the simulation settings, compared with 24 from the plane-wave model.

These comparisons indicate the success of the simulations in capturing results at near-focal positions. To further validate the accuracy of the simulation, the dependence of normalised power and polarisation of the output pulse as a function of the polarisation angle of the three input beams was investigated, which is independent of input beam profile. It is then compared with theoretical predictions. For this particular interaction geometry, a maximal output photon number is achieved when the three input beams are all polarised at 45°. This can be well reasoned for by the maximal interactions between different components of the electric and magnetic fields when they are equally distributed into two polarisation components, as suggested by the invariant term $\mathbf{E} \cdot \mathbf{B}$ present in the non-linear source terms. The resulting output pulse is also polarised at 45°. Nine simulations with the same interaction geometry were run while varying the polarisation angle γ of the three input pulses. Figure 8 shows the normalised power and polarisation of the output pulse from the simulation results and theory. The simulation results closely match the theoretical predictions for the angles

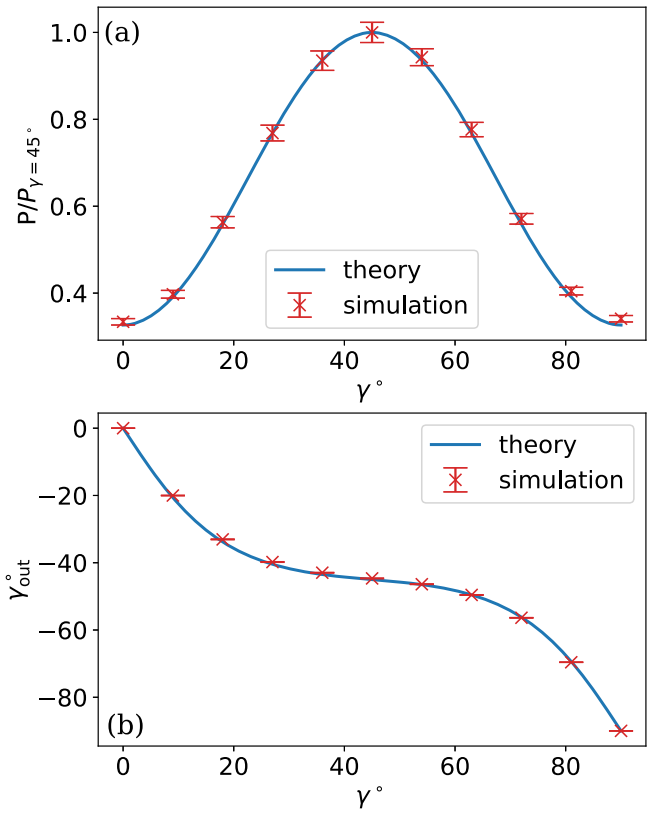

Fig. 8 | Benchmarking of the solver in four-wave mixing. The simulation results are benchmarked by investigating (**a**) the normalised power and (**b**) the polarisation angle of the output pulse as a function of the polarisation angle of input pulses. The minus sign in the output polarisation angle follows the convention used in Eq. (22). All points align well with theory within error bars (calculated as standard deviations of each quantity at a range of detector locations).

tested, validating the accuracy of the solver when applied to a different quantum phenomenon and field configuration.

Conclusions

In this paper, a semi-classical three-dimensional solver for quantum vacuum effects based on the Heisenberg-Euler Lagrangian was introduced. The solver operates on a modified Yee scheme and is integrated into the PIC framework OSIRIS. The precision and robustness of the HE QED solver in three dimensions were demonstrated by applying it to two quantum vacuum phenomena: vacuum birefringence and four-wave mixing. The results align well with analytical predictions and results from previous solvers. The time-resolved feature of the solver is also presented in real-time FFTs, the interaction region and the evolution of the output pulse. This allows one to gain unique insights into the full range of quantum signatures and structural details throughout the interaction process.

The time-resolved capability of the solver is of great potential in uncovering physics origins of quantum vacuum interactions, and translating from the quantum interpretation to classical properties. For instance, the widening diffraction cone of a probe pulse due to a momentum transfer between photons studied in ref. 54 can be analysed in greater temporal detail within a semi-classical framework. The generation and evolution of multiple harmonics in multi-beam interactions[76] can also be traced in more detail.

Looking ahead, the solver could be applied to studying interactions of novel pulse shapes, including Laguerre-Gaussian beams[22,77] and tightly focused beams[61]. The simulation results can complement existing theoretical work and provide benchmarks for future high-power laser experiments. Additionally, with the adaptation and use of a virtual detector diagnostic developed in ref. 78, in future it will be possible to assign far-field information collected by infinite-distance detectors, providing a comprehensive analysis for future high energy laser experiments. Finally, it opens up the possibility of investigating QED effects in the presence of particles. For example, in future four-wave mixing experiments, the solver could place initial estimates of noise levels from Compton scattering, thus opening the way to full-scale modelling of upcoming all-optical photon-photon scattering experiments.

Data availability

The datasets generated during the current study are available in the Figshare public repository.

Code availability

The source code of the quantum vacuum solver is available from the corresponding author on reasonable request.

Received: 21 October 2024; Accepted: 5 May 2025;
Published online: 05 June 2025

References

1. Yennie, D. R. Precision tests of QED. *AIP Conf. Proc.* **123**, 468–476 (1984).
2. Escribano, R. & Massó, E. High precision tests of QED and physics beyond the standard model. *Eur. Phys. J. C.* **4**, 139–143 (1998).
3. Gumberidze, A. et al. Precision tests of QED in strong fields: experiments on hydrogen- and helium-like uranium. *J. Phys.: Conf. Ser.* **58**, 87 (2007).
4. Heyl, J. S. & Hernquist, L. Birefringence and dichroism of the QED vacuum. *J. Phys. A: Math. Gen.* **30**, 6485 (1997).
5. Klein, J. J. & Nigam, B. P. Birefringence of the Vacuum. *Phys. Rev.* **135**, B1279–B1280 (1964).
6. Heinzl, T. et al. On the observation of vacuum birefringence. *Opt. Commun.* **267**, 318–321 (2006).
7. Karbstein, F. et al. Vacuum birefringence at x-ray free-electron lasers. *N. J. Phys.* **23**, 095001 (2021).
8. Mignani, R. P. et al. Evidence for vacuum birefringence from the first optical-polarimetry measurement of the isolated neutron star RX J1856.5-3754. *Monthly Not. R. Astronomical Soc.* **465**, 492–500 (2016).
9. Denisov, V., Dolgaya, E. & Sokolov, V. Nonperturbative qed vacuum birefringence. *J. High. Energ. Phys.* **2017**, 105 (2017).
10. Formanek, M. et al. Signatures of vacuum birefringence in low-power flying focus pulses. *Phys. Rev. D.* **109**, 056009 (2024).
11. Wistisen, T. N. & Uggerhøj, U. I. Vacuum birefringence by compton backscattering through a strong field. *Phys. Rev. D.* **88**, 053009 (2013).
12. Karbstein, F. et al. Vacuum birefringence in strong inhomogeneous electromagnetic fields. *Phys. Rev. D.* **92**, 071301 (2015).
13. Ejlli, A. et al. The pvlas experiment: A 25 year effort to measure vacuum magnetic birefringence. *Phys. Rep.* **871**, 1–74 (2020).
14. Baier, R. & Breitenlohner, P. The vacuum refraction index in the presence of external fields. *Nuovo Cim. B (1965-1970)* **47**, 117–120 (1967).
15. Becker, W. & Mitter, H. Vacuum polarization in laser fields. *J. Phys. A: Math. Gen.* **8**, 1638 (1975).
16. Tennant, D. M. Four wave mixing as a probe of the vacuum. *Phys. Rev. D.* **93**, 125032 (2016).
17. Lundin, J. et al. Analysis of four-wave mixing of high-power lasers for the detection of elastic photon-photon scattering. *Phys. Rev. A* **74**, 043821 (2006).
18. Lundström, E. et al. Using high-power lasers for detection of elastic photon-photon scattering. *Phys. Rev. Lett.* **96**, 083602 (2006).
19. King, B., Hu, H. & Shen, B. Three-pulse photon-photon scattering. *Phys. Rev. A* **98**, 023817 (2018).

20. Moulin, F. & Bernard, D. Four-wave interaction in gas and vacuum: definition of a third-order nonlinear effective susceptibility in vacuum: vacuum(3). *Opt. Commun.* **164**, 137–144 (1999).
21. MacLeod, A. J. & King, B. Fundamental constants from photon-photon scattering in three-beam collisions. *Phys. Rev. A* **110**, 032216 (2024).
22. Aboushelbaya, R. et al. Orbital angular momentum coupling in elastic photon-photon scattering. *Phys. Rev. Lett.* **123**, 113604 (2019).
23. Homma, K. Sensitivity to dark energy candidates by searching for four-wave mixing of high-intensity lasers in the vacuum. *Prog. Theor. Exp. Phys.* **2012**, 04D004 (2012).
24. Böhl, P., King, B. & Ruhl, H. Vacuum high-harmonic generation and electromagnetic shock. *J. Plasma Phys.* **82**, 655820202 (2016).
25. Baier, V. N., Milstein, A. I. & Shaisultanov, R. Z. Photon splitting in a very strong magnetic field. *Phys. Rev. Lett.* **77**, 1691–1694 (1996).
26. Adler, S. L. Photon splitting and photon dispersion in a strong magnetic field. *Ann. Phys.* **67**, 599–647 (1971).
27. Di Piazza, A., Hatsagortsyan, K. Z. & Keitel, C. H. Laser-photon merging in proton-laser collisions. *Phys. Rev. A* **78**, 062109 (2008).
28. Gies, H., Karbstein, F. & Shaisultanov, R. Laser photon merging in an electromagnetic field inhomogeneity. *Phys. Rev. D.* **90**, 033007 (2014).
29. Gies, H., Karbstein, F. & Seegert, N. Photon merging and splitting in electromagnetic field inhomogeneities. *Phys. Rev. D.* **93**, 085034 (2016).
30. Gies, H., Karbstein, F. & Seegert, N. Quantum reflection as a new signature of quantum vacuum nonlinearity. *N. J. Phys.* **15**, 083002 (2013).
31. Burke, D. L. et al. Positron production in multiphoton light-by-light scattering. *Phys. Rev. Lett.* **79**, 1626–1629 (1997).
32. Bernard, D. et al. Search for stimulated photon-photon scattering in vacuum. *Eur. Phys. J. D.* **10**, 141–145 (2000).
33. Aaboud, M. et al. Evidence for light-by-light scattering in heavy-ion collisions with the atlas detector at the lhc. *Nat. Phys.* **13**, 852–858 (2017).
34. Aad, G. et al. Observation and measurement of forward proton scattering in association with lepton pairs produced via the photon fusion mechanism at atlas. *Phys. Rev. Lett*. **125**, 261801 (2020).
35. Marklund, M. & Lundin, J. Quantum vacuum experiments using high intensity lasers. *Eur. Phys. J. D.* **55**, 319–326 (2009).
36. Robertson, S. et al. Experiment to observe an optically induced change of the vacuum index. *Phys. Rev. A* **103**, 023524 (2021).
37. Ahmadiniaz, N. et al. Letter of intent: Towards a vacuum birefringence experiment at the Helmholtz international beamline for extreme fields. *High Power Laser SCi. Eng.* **13**, e7. https://doi.org/10.48550/arXiv.2405.18063 (2025).
38. Tanaka, K. A., Spohr, K. M. & Balabanski, D. L. et al. Current status and highlights of the ELI-NP research program. *Matter Radiat. Extremes* **5**, 024402 (2020).
39. Hernandez-Gomez, C. Vulcan 20-20 upgrade. https://www.clf.stfc.ac.uk/Pages/Vulcan-2020.aspx (accessed 1 May 2025).
40. Zuegel, J. Ep-opal - planning for a next-generation laser user facility dedicated to the study of ultra-high intensity laser-matter interactions https://indico.duke.edu/event/1/contributions/60/ (2023) (accessed 1 May 2025).
41. University of Rochester, Flagship experiment selection report. https://nsf-opal.rochester.edu/documentation/ (2024) (accessed 1 May 2025).
42. Wang, X. et al. 13.4 fs, 0.1 hz OPCPA front end for the 100 PW-class laser facility. *Ultrafast Sci.* **2**, 9894358 (2022).
43. Born, M. & Infeld, L. Foundations of the New Field Theory. *Proc. R. Soc. Lond. Ser. A, Containing Pap. A Math. Phys. Character* **144**, 425–451 (1934).
44. Dehghani, A., Setare, M. R. & Zarepour, S. Self-energy problem, vacuum polarization, and dual symmetry in Born-Infeld-type U(1) gauge theories. *Eur. Phys. J.* **137**, 859 (2022).
45. Villalba-Chávez, S. & Di Piazza, A. Axion-induced birefringence effects in laser driven nonlinear vacuum interaction. *J. High. Energ. Phys.* **2013**, 136 (2013).
46. Paixão, J. M. A. et al. Probing the interference between non-linear, axionic and space-time-anisotropy effects in the QED vacuum. *J. High. Energ. Phys.* **2024**, 29 (2024).
47. Evans, S. & Schützhold, R. Searching for axion resonances in vacuum birefringence with three-beam collisions. *Phys. Rev. D.* **109**, L091901 (2024).
48. Gies, H., Jaeckel, J. & Ringwald, A. Polarized light propagating in a magnetic field as a probe for millicharged fermions. *Phys. Rev. Lett.* **97**, 140402 (2006).
49. Lundstrom, E. *Detection of elastic photon-photon scattering through four-wave coupling*. Master's thesis, Umeå University (2005).
50. Berezin, A. V. & Fedotov, A. M. Analytical formula for signal optimization in stimulated photon-photon scattering setup with three laser pulses. *Phys. Rev. D.* **110**, 016009 (2024).
51. Karbstein, F. & Sundqvist, C. Probing vacuum birefringence using x-ray free electron and optical high-intensity lasers. *Phys. Rev. D.* **94**, 013004 (2016).
52. Karbstein, F. Vacuum birefringence in the head-on collision of x-ray free-electron laser and optical high-intensity laser pulses. *Phys. Rev. D.* **98**, 056010 (2018).
53. Mosman, E. A. & Karbstein, F. Vacuum birefringence and diffraction at an x-ray free-electron laser: From analytical estimates to optimal parameters. *Phys. Rev. D.* **104**, 013006 (2021).
54. Ahmadiniaz, N. et al. Detection schemes for quantum vacuum diffraction and birefringence. *Phys. Rev. D.* **108**, 076005 (2023).
55. Karbstein, F. & Mosman, E. A. Enhancing quantum vacuum signatures with tailored laser beams. *Phys. Rev. D.* **101**, 113002 (2020).
56. Dumlu, C. K., Nakamiya, Y. & Tanaka, K. A. Qed vacuum nonlinearity in laguerre-gauss beams. *Phys. Rev. D.* **106**, 116001 (2022).
57. Lindner, A., Ölmez, B. & Ruhl, H. Numerical simulations of the nonlinear quantum vacuum in the Heisenberg-Euler weak-field expansion. *J. Comput. Phys.: X* **17**, 100124 (2023).
58. Gies, H., Karbstein, F. & Kohlfürst, C. All-optical signatures of Strong-Field QED in the vacuum emission picture. *Phys. Rev. D.* **97**, 036022 (2018).
59. Gies, H. et al. Photon-photon scattering at the high-intensity frontier. *Phys. Rev. D.* **97**, 076002 (2018).
60. Blinne, A. et al. All-optical signatures of quantum vacuum nonlinearities in generic laser fields. *Phys. Rev. D.* **99**, 016006 (2019).
61. Blinne, A. et al. The vacuum emission picture beyond paraxial approximation. *J. Phys.: Conf. Ser.* **1206**, 012017 (2019).
62. Grismayer, T. et al. Quantum Electrodynamics vacuum polarization solver. *N. J. Phys.* **23**, 095005 (2021).
63. Fonseca, R. A. et al. OSIRIS: A Three-Dimensional, Fully Relativistic Particle in Cell Code for Modeling Plasma Based Accelerators. In *Computational Science - ICCS 2002*, vol. 2331, 342–351 (2002).
64. Grismayer, T. et al. Laser absorption via quantum electrodynamics cascades in counter propagating laser pulses. *Phys. Plasmas* **23**, 056706 – 11 (2016).
65. Grismayer, T. et al. Seeded QED cascades in counterpropagating laser pulses. *Phys. Rev. E* **95**, 1135 – 8 (2017).
66. Amaro, O., Badiali, C. & Martinez, B. Neural network sampling of bethe-heitler process in particle-in-cell codes. *arXiv preprint 2406.02491* (2024).
67. Heisenberg, W. & Euler, H. Folgerungen aus der Diracschen Theorie des Positrons. *Z. Phys.* **98**, 714–732 (1936).
68. Schwinger, J. On Gauge invariance and vacuum polarization. *Phys. Rev.* **82**, 664–679 (1951).

69. Dunne, G. V. & Hall, T. M. Borel summation of the derivative expansion and effective actions. *Phys. Rev. D.* **60**, 065002 (1999).
70. Soljačić, M. & Segev, M. Self-trapping of electromagnetic beams in vacuum supported by QED nonlinear effects. *Phys. Rev. A* **62**, 043817 (2000).
71. Torres, R. *Realistic modelling of vacuum polarization induced light scattering scenarios in extreme intense fields*. Master's thesis, Técnico Lisboa (2017).
72. Saleh, B. E. A. & Teich, M. C. *Beam Optics*, chap. 3, 80–107 (John Wiley & Sons, Ltd, 1991).
73. Yee, K. Numerical solution of initial boundary value problems involving maxwell's equations in isotropic media. *IEEE Trans. Antennas Propag.* **14**, 302–307 (1966).
74. Arber, T. D. et al. Contemporary particle-in-cell approach to laser-plasma modelling. *Plasma Phys. Control. Fusion* **57**, 113001 (2015).
75. de Almeida, R. R. *Arbitrarily non-paraxial electromagnetic wave-packets in particle-in-cell codes*. Master's thesis, University of Lisbon - Instituto Superior Técnico (IST) (2023).
76. Gies, H., Karbstein, F. & Klar, L. Quantum vacuum signatures in multicolor laser pulse collisions. *Phys. Rev. D.* **103**, 076009 (2021).
77. Pampaloni, F. & Enderlein, J. Gaussian, hermite-gaussian, and laguerre-gaussian beams: A primer. *arXiv preprint 0410021* (2004).
78. Pardal, M. et al. Radio: An efficient spatiotemporal radiation diagnostic for particle-in-cell codes. *Computer Phys. Commun.* **285**, 108634 (2023).

Acknowledgements

This work was supported by the Oxford-ShanghaiTech collaboration agreement project and the John Adams Institute grant ST/V001655/1, and partially supported by FCT (Foundation for Science and Technology, Portugal) under the project X-MASER No. 2022.02230.PTDC. Z. Z acknowledges support from the Clarendon Scholarship scheme, and useful discussions with R. Almeida, P. Bilbao. T. Silva, H. Gies and F. Karbstein. The simulations were performed on computing resources provided by UKRI-STFC Scientific Computing Department's SCARF cluster.

Author contributions

Z. Z updated the solver to OSIRIS 4.0, produced the simulation results and wrote the manuscript. R. T and T. G developed the original solver and benchmarking in two dimensions, and provided vital discussions for vacuum birefringence. I. O., E. D., A. J., R. J. L. T. and M. W. V provided useful discussions for four-wave mixing. R. A supervised the project day-to-day. P. A. N and L. O. S were the principle supervisors for the project. All the authors discussed the results and reviewed the manuscript.

Competing interests

The authors declare no competing interests.

Additional information

Supplementary information The online version contains supplementary material available at https://doi.org/10.1038/s42005-025-02128-8.

Correspondence and requests for materials should be addressed to Zixin Zhang.

Peer review information *Communications Physics* thanks the anonymous reviewers for their contribution to the peer review of this work.